

Hyper-order baryon number fluctuations at finite temperature and density

Wei-jie Fu,¹ Xiaofeng Luo,² Jan M. Pawłowski,^{3,4} Fabian Rennecke,⁵ Rui Wen,¹ Nu Xu,^{2,6,7} and Shi Yin¹

¹*School of Physics, Dalian University of Technology, Dalian, 116024, P.R. China*

²*Key Laboratory of Quark & Lepton Physics (MOE) and Institute of Particle Physics, Central China Normal University, Wuhan 430079, China*

³*Institut für Theoretische Physik, Universität Heidelberg, Philosophenweg 16, 69120 Heidelberg, Germany*

⁴*ExtreMe Matter Institute EMMI, GSI, Planckstraße 1, D-64291 Darmstadt, Germany*

⁵*Physics Department, Brookhaven National Laboratory, Upton, NY 11973, USA*

⁶*Lawrence Berkeley National Laboratory, Berkeley, CA 94720, USA*

⁷*Institute of Modern Physics of CAS, Lanzhou 730000, China*

We study the generalized susceptibilities from kurtosis which is known as the χ_4^B/χ_2^B to the χ_8^B/χ_2^B . The results are obtained under the finite temperature and baryon density. We give the comparison of our results with the lattice QCD results under the vanishing μ_B . We get the numerical results under the Polyakov-quark-meson (PQM) model with the functional renormalisation group (FRG) approach.

PACS numbers: 11.30.Rd, 11.10.Wx, 05.10.Cc, 12.38.Mh

I. INTRODUCTION

Lots of effort have been made to study the QCD phase structure at finite temperature and density over the last few decades, both from the experimental and theoretical sides [1–4]. One of the most intriguing open questions concerning the QCD phase diagram is the existence of the critical end point (CEP) [5], which is assumed to be located at the end of the first-order phase transition line in the $T - \mu_B$ phase diagram. Here T and μ_B are referred to the temperature and baryon chemical potential, respectively. In view of the uniqueness and importance of CEP, pinning down its location has played a pivotal role in understanding phases of strongly interacting nuclear matter under extreme conditions. Note that the phase transition at CEP is of genuine second order, and thus the correlation length ξ diverges at this point in the thermodynamic limit. Consequently, critical observables, such as fluctuations of conserved charges that receive contributions in powers of ξ from critical dynamics in the proximity of CEP [6], are employed to explore the location of CEP [1, 7].

Within the Beam Energy Scan (BES) Program at the Relativistic Heavy Ion Collider (RHIC), significant fluctuation measurements have been performed in Phase I, involving the skewness and kurtosis of the net-proton, net-charge, net-kaon multiplicity distributions [8–11], second-order off-diagonal cumulants, i.e., correlations of net-proton, net-charge, net-kaon multiplicity distributions [12]. Remarkably, very recently the STAR collaboration has reported the first evidence of a non-monotonic variation in kurtosis \times variance of the net-proton number distribution as a function of the collision energy with 3.0σ significance for central collisions [7]. Moreover, the measurement has also been extended to the sixth-order cumulant of net-proton and net-charge distributions, and preliminary results have been obtained [13, 14].

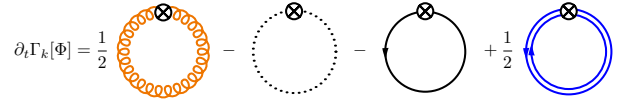


FIG. 1. Diagrammatic representation of the QCD flow equation within the fRG approach. Lines of different types on the r.h.s. of the equation stand for the full propagators of gluon, ghost, quark, and meson, respectively. Note that the mesonic degree of freedom is denoted by double lines with opposite arrows. The crossed circles represent the regulators in the flow equation.

II. QCD AND LOW ENERGY EFFECTIVE THEORIES WITHIN THE FRG APPROACH

An generic Euclidian quantum field theory is completely described by its effective action $\Gamma[\Phi]$, where Φ is used to denote an aggregate of all fields in the theory. In the fRG approach, this full quantum effective action is resolved by interpolating it as a function of a renormalization group (RG) scale k , i.e., $\Gamma_k[\Phi]$, successively, starting from the respective classical action $S[\Phi]$ at a very high ultraviolet (UV) scale, say Λ , towards the infrared (IR) limit $k \rightarrow 0$ with $\Gamma[\Phi] = \Gamma_{k=0}[\Phi]$. For more details about the formalism of fRG, see, e.g., [15] as well as [16, 17].

To be specific, the flow equation for QCD, which describes the evolution of its effective action with the RG scale k , is shown in Fig. 1 diagrammatically. As one could see, the QCD flow receives contributions not only from the gluon, ghost and the quark, i.e., the fundamental partonic degrees of freedom in QCD, but also from hadrons, such as mesons, which are composite or emergent degrees of freedom, and are generated dynamically through strong interactions when the RG scale is reduced down to the nonperturbative regime of the low energy QCD. Recent first-principle QCD calculations within fRG indicate that this transition, from the partonic to composite de-

degrees of freedom, takes place in a narrow regime located at $k \sim 1$ GeV [4, 18–20]. The flow of the QCD effective action corresponding to the diagrams in Fig. 1 can be written as follows,

$$\begin{aligned} \partial_t \Gamma_k[\Phi] = & \frac{1}{2} \text{Tr} \left(G_{AA,k} \partial_t R_{A,k} \right) - \text{Tr} \left(G_{c\bar{c},k} \partial_t R_{c,k} \right) \\ & - \text{Tr} \left(G_{q\bar{q},k} \partial_t R_{q,k} \right) + \frac{1}{2} \text{Tr} \left(G_{\phi\phi,k} \partial_t R_{\phi,k} \right), \end{aligned} \quad (1)$$

with $\Phi = (A, c, \bar{c}, q, \bar{q}, \phi)$, where G 's and R 's are the propagators and regulators of different fields, respectively. Note that the scale dependence of these quantities is explicitly indicated with a suffix k . The RG time in Eq. (1) is defined by $t = \ln(k/\Lambda)$, with the initial UV scale Λ . We are not going to discuss details of the QCD flow in Eq. (1) here, and interested readers are strongly suggested to refer to, e.g., [4, 18–26] for recent progress in understanding of QCD or Yang-Mills theory in the vacuum and at finite temperature and density within the fRG approach, and also [27–33] for QCD related review articles of fRG.

As mentioned above, the transition of the degrees of freedom, from the partonic ones in the perturbative regime of high energy to the hadronic ones in the non-perturbative region of low energy, is realized through the dynamical hadronization in the fRG approach. With the help of the technique of dynamical hadronization, composite operators of resonated channels, e.g., the σ - π channel, i.e., the scalar-pseudoscalar one in the low energy QCD, which are most relevant to the dynamics of the system, are bosonized or Hubbard-Stratonovich transformed successively with the evolution of RG scale. For more details, see, e.g., [4, 28, 34–36].

In a recent first-principle fRG calculation to QCD, it has been shown clearly that a sequential decoupling of the gluon, quark, and mesonic degrees of freedom from the system with decreasing RG scale, results in a natural emergence of the low energy effective theory (LEFT) when the scale $k \lesssim 1$ GeV [4]. The fRG formalism is ideally suited to the description of a phenomenon of emergence, which usually involves energy scale of different hierarchies, characteristic to different degrees of freedom. When the scale k is high and the system is located in the perturbative region, the only relevant degrees of freedom in QCD are the gluon and quark, and the hadronic or mesonic ones are irrelevant due to their large masses. When k decreases below ~ 1 GeV, the gluon develops a significant mass gap in the low momentum region, and thus decouples from the system. The dynamics is taken over by the emergent composite degrees of freedom, e.g. mesons, in particular the π meson, which is in essence the Goldstone boson related to the spontaneously breaking chiral symmetry in the low energy QCD, and is the lightest hadron of mass ~ 140 MeV in the vacuum.

The direct consequence of the natural emergence of LEFT is that, if the flow equation of QCD in Eq. (1) is evolved at a starting scale, in which the glue sector

has already significantly been suppressed by the gluon mass gap, say $\Lambda \sim 1$ GeV, it is safe and legitimate to disregard quantum fluctuations of the glue sector, i.e., the first two diagrams in Fig. 1. Hence we are left with a scale dependent effective action, only composed of the matter sector fields, namely, the quark and meson, which reads

$$\begin{aligned} \Gamma_k[\Phi] = & \int_x \left\{ Z_{q,k} \bar{q} \left[\gamma_\mu \partial_\mu - \gamma_0 (\hat{\mu} + igA_0) \right] q + \frac{1}{2} Z_{\phi,k} (\partial_\mu \phi)^2 \right. \\ & \left. + h_k \bar{q} (T^0 \sigma + i \gamma_5 \vec{T} \cdot \vec{\pi}) q + V_k(\rho, A_0) - c\sigma \right\}, \end{aligned} \quad (2)$$

with a reduction of the involved species of fields $\Phi = (q, \bar{q}, \phi)$, and the shorthand notation for the space-time integral $\int_x = \int_0^{1/T} dx_0 \int d^3x$. Note that in this work we only consider the case of $N_f = 2$ flavor quark, i.e., the quark field $q = (u, d)^T$ in the action Eq. (2). The meson field $\phi = (\sigma, \vec{\pi})$, being in the adjoint representation of group $U_V(N_f) \times U_A(N_f)$ in the flavor space, is coupled with the quark field through the Yukawa coupling. Here T^0 and T^i 's ($i = 1, 2, \dots, N_f^2 - 1$) are the generators of $U(N_f)$ group, denoted collectively as T^a 's, with the normalization $\text{Tr}(T^a T^b) = \frac{1}{2} \delta^{ab}$, which yields $T^0 = \frac{1}{\sqrt{2N_f}} \mathbb{1}_{N_f \times N_f}$. $Z_{q,k}$ and $Z_{\phi,k}$ are the wave function renormalization for the quark and meson fields, respectively. Note that the wave function renormalizations, as well as the Yukawa coupling h_k and the effective potential V_k to be discussed in the following, are dependent on the RG scale k .

Quantum fluctuations of the glue sector are suppressed in the low energy region due to the large gluon mass gap as discussed above, and consequently it is reasonable to neglect their corresponding contributions in the flow equation of QCD in Fig. 1 or Eq. (1). The gluonic background field is, however, of significant importance for the QCD thermodynamics. In Eq. (2) the temporal component of the gluonic background field A_0 is encoded, which is responsible for the quark confinement in the statistical sense of thermodynamics, see, e.g., [37–40] for more details. Therefore, the effective potential in Eq. (2) reads

$$V_k(\rho, A_0) = V_{\text{glue},k}(A_0) + V_{\text{mat},k}(\rho, A_0), \quad (3)$$

where the first term on the right-hand side is due to the temporal gluonic background field A_0 , which can also be formulated in terms of the Polyakov loop $L(A_0)$. More details about $V_{\text{glue},k}$ used in this work can be found in Appendix A. The matter part of the effective potential $V_{\text{mat},k}$ arises from the quark and meson diagrams in Fig. 1, which is dependent on the meson field through $\rho = \phi^2/2$. Clearly, $V_{\text{mat},k}$ is $SU_A(2)$ or $O(4)$ invariant, which guarantees that the chiral symmetry is preserved on the level of interactions. The explicit breaking of the chiral symmetry is attributed to the linear term $-c\sigma$ in Eq. (2), which is also related to a nonvanishing value of

the current quark mass. The quark chemical potential $\hat{\mu} = \text{diag}(\mu_u, \mu_d)$ in the first line of Eq. (2) is a diagonal matrix in the flavor space, and $\mu = \mu_u = \mu_d$ is assumed throughout this work. The quark chemical potential is related to the baryon chemical potential via $\mu = \mu_B/3$.

In the scale regime of LEFT, as we have discussed above, the flow equation of the effective action in Eq. (1) is reduced to

$$\partial_t \Gamma_k[\Phi] = -\text{Tr}\left(G_{q\bar{q},k} \partial_t R_{q,k}\right) + \frac{1}{2} \text{Tr}\left(G_{\phi\phi,k} \partial_t R_{\phi,k}\right), \quad (4)$$

where $R_{q,k}$ and $R_{\phi,k}$ are the regulators for the quark and meson fields, respectively. In this work we employ the $3d$ -flat regulators, as follows

$$R_{\phi,k}(q_0, \mathbf{q}) = Z_{\phi,k} \mathbf{q}^2 r_B(\mathbf{q}^2/k^2), \quad (5)$$

$$R_{q,k}(q_0, \mathbf{q}) = Z_{q,k} i\gamma \cdot \mathbf{q} r_F(\mathbf{q}^2/k^2), \quad (6)$$

with

$$r_B(x) = \left(\frac{1}{x} - 1\right) \Theta(1-x), \quad (7)$$

$$r_F(x) = \left(\frac{1}{\sqrt{x}} - 1\right) \Theta(1-x), \quad (8)$$

where $\Theta(x)$ denotes the Heaviside step function. The full propagators read

$$G_{q\bar{q}/\phi\phi,k} = \left(\frac{1}{\Gamma_k^{(2)}[\Phi] + R_k} \right)_{q\bar{q}/\phi\phi}, \quad (9)$$

with $\Gamma_k^{(2)}[\Phi] = \delta^2 \Gamma_k[\Phi] / (\delta\Phi_{i_1} \delta\Phi_{i_2})$, where different species of fields are distinguished with the help of the subscripts in Φ_{i_1/i_2} . Inserting the effective action (2) into the flow equation (4), one is led to the flow equation for the effective potential of the matter sector, as follows

$$\begin{aligned} \partial_t V_{\text{mat},k}(\rho) = & \frac{k^4}{4\pi^2} \left[(N_f^2 - 1) l_0^{(B,4)}(\tilde{m}_{\pi,k}^2, \eta_{\phi,k}; T) \right. \\ & + l_0^{(B,4)}(\tilde{m}_{\sigma,k}^2, \eta_{\phi,k}; T) \\ & \left. - 4N_c N_f l_0^{(F,4)}(\tilde{m}_{q,k}^2, \eta_{q,k}; T, \mu) \right], \quad (10) \end{aligned}$$

where the threshold functions $l_0^{(B/F,4)}$ as well as other threshold functions in the following can be found in e.g., [4, 41], and the dimensionless renormalized quark and meson masses read

$$\tilde{m}_{q,k}^2 = \frac{h_k^2 \rho}{2k^2 Z_{q,k}^2}, \quad \tilde{m}_{\pi,k}^2 = \frac{V'_{\text{mat},k}(\rho)}{k^2 Z_{\phi,k}}, \quad (11)$$

$$\tilde{m}_{\sigma,k}^2 = \frac{V'_{\text{mat},k}(\rho) + 2\rho V''_{\text{mat},k}(\rho)}{k^2 Z_{\phi,k}}. \quad (12)$$

The anomalous dimensions for the quark and meson fields in Eq. (10) are defined as

$$\eta_{q,k} = -\frac{\partial_t Z_{q,k}}{Z_{q,k}}, \quad \eta_{\phi,k} = -\frac{\partial_t Z_{\phi,k}}{Z_{\phi,k}}, \quad (13)$$

respectively. Accordingly, projecting the flow in Eq. (4) onto the one-particle irreducible (1PI) two-point function of the meson, it is readily obtained that

$$\eta_{\phi,k} = -\frac{1}{3Z_{\phi,k}} \delta_{ij} \frac{\partial}{\partial(|\mathbf{p}|^2)} \frac{\delta^2 \partial_t \Gamma_k}{\delta\pi_i(-p) \delta\pi_j(p)} \Big|_{\substack{p_0=0 \\ \mathbf{p}=0}}, \quad (14)$$

where the spacial component is employed. Note that in the case of finite temperature and density, the $O(4)$ rotation symmetry in the $4-d$ Euclidean space is broken, and as a matter of fact, the mesonic anomalous dimension extracted above is different from that projected onto the temporal component. In another word, $\eta_{\phi,k}$ is split into $\eta_{\phi,k}^\perp$ and $\eta_{\phi,k}^\parallel$, which are transverse and longitudinal to the heat bath, respectively, at finite temperature and density. The influences of the splitting of $\eta_{\phi,k}$ on the thermodynamics and baryon number fluctuations have been investigated in detail [41], and it has been found that the impact is small. Therefore, it is reasonable to disregard the splitting of anomalous dimensions, and $\eta_{\phi,k} = \eta_{\phi,k}^\perp = \eta_{\phi,k}^\parallel$, as well as that for the quark anomalous dimension in the following, is assumed throughout this work. In the same way, the quark anomalous dimension is obtained by projecting the relevant flow onto the vector channel of the 1PI quark-antiquark correlation function, as follows

$$\begin{aligned} \eta_q = & \frac{1}{4Z_{q,k}} \\ & \times \text{Re} \left[\frac{\partial}{\partial(|\mathbf{p}|^2)} \text{tr} \left(i\gamma \cdot \mathbf{p} \left(-\frac{\delta^2}{\delta\bar{q}(p) \delta q(p)} \partial_t \Gamma_k \right) \right) \right] \Big|_{\substack{p_0, ex \\ \mathbf{p}=0}}, \quad (15) \end{aligned}$$

where the external spacial momentum is chosen to be zero as same as the mesonic one, since the vanishing momentum is most relevant to the flow of effective potential in Eq. (10). Note that the lowest mode of the fermionic Matsubara frequency is nonvanishing and we designate it here as $p_{0,ex}$, to be described in Appendix B. Moreover, the expression in the square bracket in (15) is complex-valued, rather than real, when the chemical potential is nonzero. This artifact stems from the naive truncation of the external frequency, that is resolved through a resummation of the external frequency of quark [42]. The flow equation of the Yukawa coupling is readily obtained via the projection of the 1PI quark-antiquark correlation function on the scalar channel, which reads

$$\partial_t h_k = \frac{1}{2\sigma} \text{Re} \left[\text{tr} \left(-\frac{\delta^2}{\delta\bar{q}(p) \delta q(p)} \partial_t \Gamma_k \right) \right] \Big|_{\substack{p_0, ex \\ \mathbf{p}=0}}. \quad (16)$$

The explicit expressions for the meson and quark anomalous dimensions, and the flow of the Yukawa coupling can be found in Appendix B.

III. THERMODYNAMICS AND HYPER-ORDER BARYON NUMBER FLUCTUATIONS

The thermodynamical potential density in the LEFT at finite temperature and nonzero baryon chemical potential is readily obtained from the effective action in Eq. (2), which reads

$$\Omega[T, \mu_B] = V_{\text{glue}}(L, \bar{L}) + V_{\text{mat}, k=0}(\rho) - c\sigma, \quad (17)$$

where the gluonic background field A_0 has been reformulated in terms of the Polyakov loop L and its complex conjugate \bar{L} . The matter sector of the effective potential is integrated out towards the IR limit $k = 0$, while the glue sector is independent of k , see Appendix A. Note that the Polyakov loop and the meson field are on their respective equations of motion, and the effective potential in Eq. (17) is normalized to zero in vacuum. The pressure of the system is directly related to the thermodynamical potential, as follows

$$p = -\Omega[T, \mu_B]. \quad (18)$$

The generalized susceptibility of the baryon number χ_n^B is defined through the n -order derivative of the pressure w.r.t. the baryon chemical potential, to wit,

$$\chi_n^B = \frac{\partial^n}{\partial(\mu_B/T)^n} \frac{p}{T^4}. \quad (19)$$

The generalized susceptibilities are related to various cumulants of the baryon number distribution, which can be measured in heavy-ion collision experiments through the cumulants of its proxy, i.e., the net proton distribution, see, e.g. [1] for details. For the lowest four orders, one is led to

$$\chi_1^B = \frac{1}{VT^3} \langle N_B \rangle, \quad \chi_2^B = \frac{1}{VT^3} \langle (\delta N_B)^2 \rangle, \quad (20)$$

$$\chi_3^B = \frac{1}{VT^3} \langle (\delta N_B)^3 \rangle, \quad (21)$$

$$\chi_4^B = \frac{1}{VT^3} \left(\langle (\delta N_B)^4 \rangle - 3 \langle (\delta N_B)^2 \rangle^2 \right), \quad (22)$$

with $\langle \dots \rangle$ denoting the ensemble average and $\delta N_B = N_B - \langle N_B \rangle$. Thus the mean value of the net baryon number of the system is given by $M = VT^3 \chi_1^B$, the variance $\sigma^2 = VT^3 \chi_2^B$, skewness $S = \chi_3^B / (\chi_2^B \sigma)$, and the kurtosis $\kappa = \chi_4^B / (\chi_2^B \sigma^2)$, respectively.

In this work emphasis is, however, put on the baryon number fluctuations of order higher than the fourth, i.e., χ_n^B 's ($n > 4$), which are named hyper-order baryon number fluctuations. As same as the low-order ones, the

hyper-order susceptibilities are also connected to their respective cumulants, and their relations, taking the fifth through eighth ones for instance, are given as follows

$$\chi_5^B = \frac{1}{VT^3} \left(\langle (\delta N_B)^5 \rangle - 10 \langle (\delta N_B)^2 \rangle \langle (\delta N_B)^3 \rangle \right), \quad (23)$$

$$\chi_6^B = \frac{1}{VT^3} \left(\langle (\delta N_B)^6 \rangle - 15 \langle (\delta N_B)^4 \rangle \langle (\delta N_B)^2 \rangle - 10 \langle (\delta N_B)^3 \rangle^2 + 30 \langle (\delta N_B)^2 \rangle^3 \right), \quad (24)$$

$$\chi_7^B = \frac{1}{VT^3} \left(\langle (\delta N_B)^7 \rangle - 21 \langle (\delta N_B)^5 \rangle \langle (\delta N_B)^2 \rangle - 35 \langle (\delta N_B)^4 \rangle \langle (\delta N_B)^3 \rangle + 210 \langle (\delta N_B)^3 \rangle \langle (\delta N_B)^2 \rangle^2 \right), \quad (25)$$

$$\chi_8^B = \frac{1}{VT^3} \left(\langle (\delta N_B)^8 \rangle - 28 \langle (\delta N_B)^6 \rangle \langle (\delta N_B)^2 \rangle - 56 \langle (\delta N_B)^5 \rangle \langle (\delta N_B)^3 \rangle - 35 \langle (\delta N_B)^4 \rangle^2 + 420 \langle (\delta N_B)^4 \rangle \langle (\delta N_B)^2 \rangle^2 + 560 \langle (\delta N_B)^3 \rangle^2 \langle (\delta N_B)^2 \rangle - 630 \langle (\delta N_B)^2 \rangle^4 \right). \quad (26)$$

IV. NUMERICAL RESULTS AND DISCUSSIONS

In this section we would like to present our calculated results and compare them with the relevant lattice calculations. Implications of our prediction for the hyper-order baryon number fluctuations in the heavy-ion collision experiments will also be discussed. But before we do that, the scales in the LEFT and OCD have to be matched.

A. Matching the scales in LEFT and OCD

Usually the scale in LEFT and that in QCD do not agree with each other exactly, and a direct consequence is that the pseudocritical temperature of the chiral phase crossover, i.e., the value of T_c at $\mu_B = 0$ is different in the LEFT and QCD. Although it is not a real phase transition, the benchmark value of T_c is well determined through, e.g., the chiral condensate, chiral susceptibilities, etc. Recently, two lattice collaborations, the HotQCD collaboration and the Wuppertal-Budapest collaboration find $T_c = 156.5 \pm 1.5$ MeV [47] and $T_c = 158.0 \pm 0.6$ MeV, respectively. Furthermore, the scale is also affected by the number of quark flavors. As shown

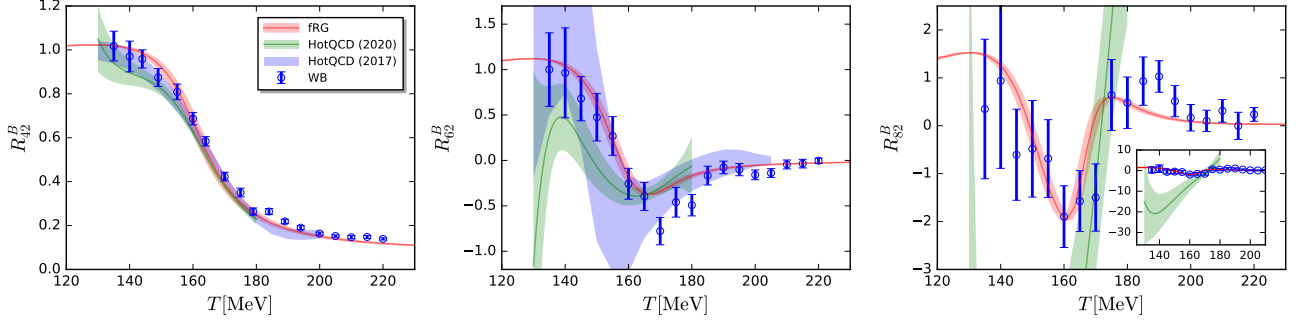


FIG. 2. $R_{42}^B = \chi_4^B / \chi_2^B$ (left panel), $R_{62}^B = \chi_6^B / \chi_2^B$ (middle panel), and $R_{82}^B = \chi_8^B / \chi_2^B$ (right panel) as functions of the temperature with vanishing baryon chemical potential ($\mu_B = 0$). Results obtained with the low energy effective theory within fRG approach are compared with lattice results from the HotQCD collaboration [43–45] and the Wuppertal-Budapest collaboration [46]. The inset in the plot of R_{82}^B shows its zoom-out view.

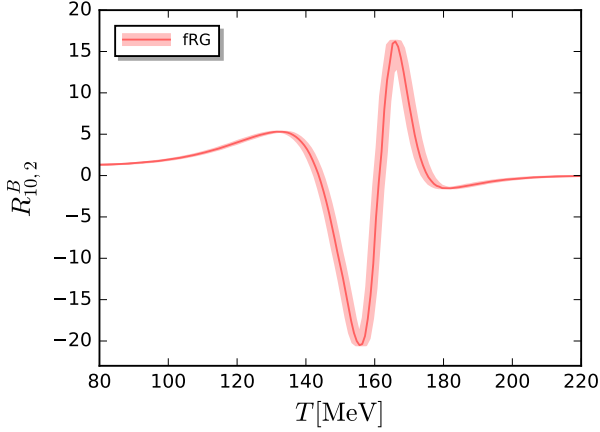


FIG. 3. $R_{10,2}^B = \chi_{10}^B / \chi_2^B$ as a function of the temperature with $\mu_B = 0$, predicted by the LEFT within the fRG approach.

in the effective action in Eq. (2), only the $N_f = 2$ flavor quarks, i.e., light quarks u and d , are included in the LEFT in this work, while in lattice simulations besides the light quarks, dynamics of the strange quark is also taken into account. Thus there should be a mismatch of the scale resulting from the different systems of $N_f = 2$ and $N_f = 2 + 1$ flavor quarks.

We denote the temperature and the baryon chemical potential in the LEFT as T_{LEFT} and μ_{BLEFT} , respectively, where the suffix is used to distinguish them from T and μ_B in QCD or lattice simulations. In order to resolve the mismatch of the scale in LEFT and QCD, a simple linear relation between them both for the temperature and chemical potential is assumed, to wit,

$$T_{LEFT} = c_T T, \quad \mu_{BLEFT} = c_\mu \mu_B, \quad (27)$$

where the constant coefficients c_T and c_μ are to be determined.

The coefficient c_T in Eq. (27) is fixed through fitting the LEFT curve of $R_{42}^B = \chi_4^B / \chi_2^B$ in the left panel of

Fig. 2, i.e., the kurtosis of the baryon number distribution $\kappa\sigma^2 = R_{42}^B$, as a function of the physical temperature T with $\mu_B = 0$ in comparison to the lattice results. It is found that the LEFT within fRG provides the best description of the lattice $\kappa\sigma^2$ with $c_T = 1.247(12)$. To proceed, the constant c_μ in Eq. (27) is determined by the curvature of the phase boundary, which is defined as the quadratic expansion coefficient of the pseudocritical temperature as a function of the baryon chemical potential around $\mu_B = 0$, i.e.,

$$\frac{T_c(\mu_B)}{T_c} = 1 - \kappa \left(\frac{\mu_B}{T_c} \right)^2 + \lambda \left(\frac{\mu_B}{T_c} \right)^4 + \dots, \quad (28)$$

with the curvature κ , where the next fourth order expansion coefficient λ is neglected in our calculations, since it hardly plays any role in the region of baryon chemical potential concerned in this work, e.g., up to $\mu_B \sim 400$ MeV in the following, due to its small value. T_c in Eq. (28) is the pseudocritical temperature at $\mu_B = 0$. Note that the curvature is invariant only if the chemical potential and temperature are rescaled with the same value, and thus the curvature κ_{LEFT} in the LEFT would not be modified if one has $c_\mu = c_T$ in Eq. (27). By employing the order parameter of the chiral phase transition, i.e., the expectation value of the sigma field $\langle \sigma \rangle$ in Eq. (2), we obtain $\kappa_{LEFT} = 0.0193$ in the $N_f = 2$ flavor LEFT. For more discussions about the phase boundary and curvature, see, e.g., [4]. This value of κ_{LEFT} is a bit larger than recent $N_f = 2 + 1$ lattice results, e.g., $\kappa = 0.015(4)$ in [47], $\kappa = 0.0149(21)$ in [48], $\kappa = 0.0153(18)$ in [49]. This mismatch of the curvature between the LEFT and lattice QCD, however, is cured through a suitable choice for the ratio c_μ / c_T in Eq. (27), and one readily arrives at

$$c_\mu = c_T \left(\frac{\kappa}{\kappa_{LEFT}} \right)^{1/2}. \quad (29)$$

Substituting $\kappa_{LEFT} = 0.0193$, $\kappa = 0.0153(18)$, and $c_T = 1.247(12)$ into the equation above, one obtains $c_\mu = 1.110(66)$.

To sum up, in this section the scales between the LEFT and QCD have been matched by resorting to two observables, i.e., R_{42}^B as a function of T at vanishing chemical potential and the curvature of phase boundary κ , which are both quite relevant to predictions of the hyper-order baryon number fluctuations at finite temperature and densities, to be discussed in the following.

B. Hyper-order baryon number fluctuations

As we have discussed above, the LEFT has been calibrated by use of the curvature of phase boundary and the kurtosis of baryon number distribution as a function of T with $\mu_B = 0$, via a detailed comparison with recent lattice results. Consequently, one could use the LEFT to make predictions for the dependence of R_{42}^B on the chemical potential, as well as the hyper-order baryon number fluctuations at finite temperature and density. In the middle and right panels of Fig. 2, $R_{62}^B = \chi_6^B/\chi_2^B$ and $R_{82}^B = \chi_8^B/\chi_2^B$ are shown versus the temperature with vanishing μ_B , respectively, and in the same way the LEFT and lattice QCD results are compared. Apparently, one observes that, with the increase of the order of fluctuations, errors of lattice calculation increase dramatically. Specifically, the eighth-order fluctuations R_{82}^B obtained by the two collaborations show a significant quantitative difference, although they are roughly consistent with each other qualitatively. It is found that the predicted hyper-order baryon number fluctuations from the LEFT within the fRG, are in qualitative agreement with both lattice results, and even consistent with the Wuppertal-Budapest result quantitatively within the errors. Moreover, we have also computed baryon number fluctuations of orders even up to the tenth in the LEFT, and the relevant result $R_{10,2}^B = \chi_{10}^B/\chi_2^B$ is presented in Fig. 3, where the chemical potential is chosen to be vanishing. Note that no lattice results for the tenth-order fluctuation are available for the moment, and the dependence of $R_{10,2}^B$ on the temperature in Fig. 3 is a pure prediction by the LEFT within the fRG approach, which needs to be confirmed by other calculations, e.g., lattice QCD, in the future.

To proceed, we consider the chemical potential dependence of baryon number fluctuations. Expanding the pressure in Eq. (18) in powers of $\hat{\mu}_B \equiv \mu_B/T$ around $\hat{\mu}_B = 0$, one is led to

$$\frac{p}{T^4} = \frac{p}{T^4} \Big|_{\hat{\mu}_B=0} + \sum_{i=1}^{\infty} \frac{\chi_{2i}^B|_{\hat{\mu}_B=0}}{(2i)!} \hat{\mu}_B^{2i}. \quad (30)$$

Truncating the Taylor expansion above up to order of $\hat{\mu}_B^8$ and employing Eq. (19), we obtain the expanded baryon

number fluctuations in the first several orders, to wit,

$$\begin{aligned} \chi_2^B &\simeq \chi_2^B|_{\hat{\mu}_B=0} + \frac{\chi_4^B|_{\hat{\mu}_B=0}}{2!} \hat{\mu}_B^2 + \frac{\chi_6^B|_{\hat{\mu}_B=0}}{4!} \hat{\mu}_B^4 \\ &\quad + \frac{\chi_8^B|_{\hat{\mu}_B=0}}{6!} \hat{\mu}_B^6, \end{aligned} \quad (31)$$

$$\chi_4^B \simeq \chi_4^B|_{\hat{\mu}_B=0} + \frac{\chi_6^B|_{\hat{\mu}_B=0}}{2!} \hat{\mu}_B^2 + \frac{\chi_8^B|_{\hat{\mu}_B=0}}{4!} \hat{\mu}_B^4, \quad (32)$$

$$\chi_6^B \simeq \chi_6^B|_{\hat{\mu}_B=0} + \frac{\chi_8^B|_{\hat{\mu}_B=0}}{2!} \hat{\mu}_B^2. \quad (33)$$

In Fig. 4 we show the lattice results χ_4^B/χ_2^B and χ_6^B/χ_2^B based on the Taylor expansion above, and the fluctuations at vanishing chemical potential, viz. $\chi_i^B|_{\hat{\mu}_B=0}$ ($i = 2, 4, 6, 8$) and relevant results in Fig. 2, from the HotQCD collaboration [45] and the Wuppertal-Budapest collaboration [46]. Moreover, χ_n^B 's in Eq. (19) could also be computed directly in the LEFT within the fRG approach, without resorting to the Taylor expansion, and the relevant results are presented in Fig. 4 for comparison. Here we choose two values of the temperature, and as expected, the LEFT result for the dependence of R_{42}^B and R_{62}^B on the chemical potential, agrees with both lattice results qualitatively, and is even quantitatively consistent with the Wuppertal-Budapest result. Moreover, it is of high interest to investigate the convergence of Taylor expansion in Eqs. (31) (32) (33), via a comparison to the full calculation of baryon number fluctuations in Eq. (19). We have done both calculations in the LEFT-fRG approach, and the relevant results are shown in Fig. 5. One observes that the Taylor expansion agrees well with the full calculation for R_{42}^B with μ_B/T going up to 1.2, but the convergence is less pronounced for the higher-order fluctuation R_{62}^B , and there is a sizable difference between these two calculations even $\mu_B/T \sim 0.8$, as shown in the right panel of Fig. 5.

In Fig. 6 R_{42}^B , R_{62}^B and R_{82}^B are depicted as functions of T with several values of μ_B , which are calculated in LEFT with the fRG approach. Relevant results in Fig. 2 for $\mu_B = 0$ are presented as well, in order to highlight effects of the finite baryon chemical potential, whose value is increased from zero to 400 MeV. One observes that both the magnitude and error of the fluctuations, in particular the high-order ones, grow with the increasing chemical potential. Due to the rapid increase of error for very high-order fluctuations at large baryon chemical potential, e.g., R_{82}^B with $\mu_B \gtrsim 200$ MeV, it is reasonable to expect that the LEFT is losing its capability of making predictions in these regimes.

In the following we would like to confront theoretical predictions on the baryon number fluctuations with experimental measurement. Frankly speaking, a direct comparison between the theory and experiment is a challenging task, or even impossible within the setup in this work. This is due to the fact that experimental data are affected by many factors, e.g., acceptance of the detec-

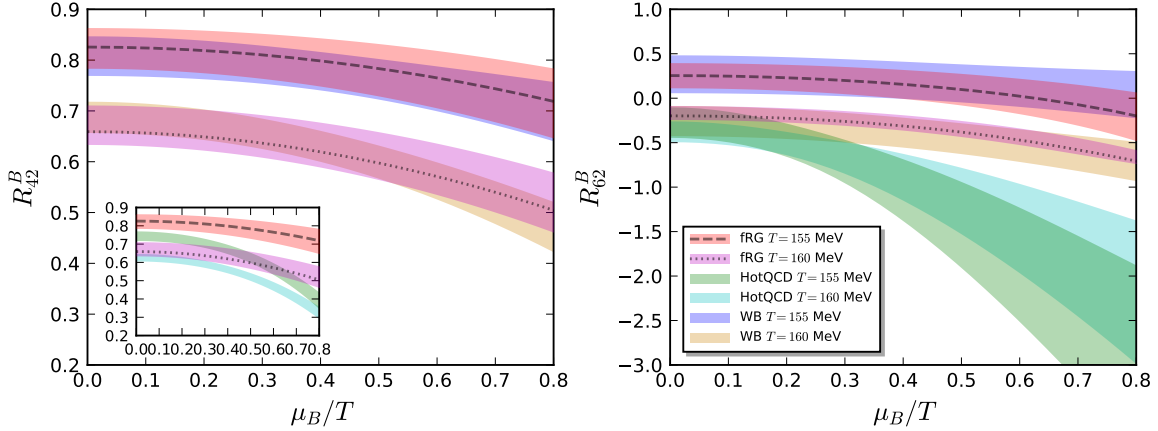


FIG. 4. R_{42}^B (left panel) and R_{62}^B (right panel) as functions of μ_B/T with $T = 155$ MeV and $T = 160$ MeV. Calculation of LEFT within the fRG approach is compared with lattice QCD by the HotQCD collaboration [45] and the Wuppertal-Budapest collaboration [46]. Note that the comparison of R_{42}^B between HotQCD and LEFT is presented in the inlay of left panel, in order to improve the readability of presentation.

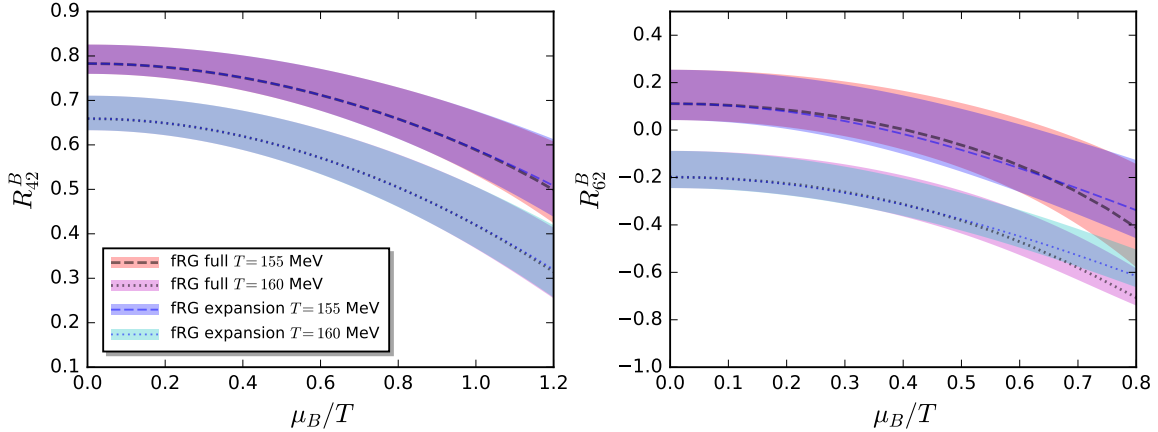


FIG. 5. Comparison between the direct full calculation of baryon number fluctuations R_{42}^B (left panel) and R_{62}^B (right panel) via Eq. (19) and the Taylor expansion in Eqs. (31) (32) (33). Both calculations are performed within the LEFT-fRG approach, and R_{42}^B , R_{62}^B are plotted as functions of μ_B/T with $T = 155$ MeV and $T = 160$ MeV.

$\sqrt{s_{NN}}$ [GeV]	200	62.4	54.4	39	27	19.6	14.5	11.5	7.7
$\mu_{B_{CF}}$ [MeV]	22	68	78	106	148	196	252	303	406
T_{CF} (I) [MeV]	158	158	158	158	157	156	153	150	138
T_{CF} (II) [MeV]	162	163	163	161	159	156	151	145	134

TABLE I. Chemical freeze-out parameters $\mu_{B_{CF}}$ and T_{CF} (freeze-out: I, II) for different center-of-mass energies per nucleon pair $\sqrt{s_{NN}}$. See text for details.

tor such as the transverse momentum p_T range, rapidity window and the centrality dependence [7, 8, 10, 13, 14], cf. also [1, 51] for more details, volume fluctuations [52],

global baryon number conservation [53, 54], resonance decays [55], etc. They constitute the non-critical contributions to fluctuation observables in experiments, and pinning down their contributions plays a pivotal role in identifying the critical signals in the BES experiment. Additionally, more important is that the critical fluctuations in heavy ion collision take place in a dynamical process, rather not static, which necessitates a theoretical description of dynamics of critical fluctuations, with dynamical evolution and nonequilibrium effects encoded. For more details about recent progress on the dynamics of critical fluctuations in QCD, see [56] and references therein.

In this work we will not take into account the non-critical and dynamical effects discussed above when the

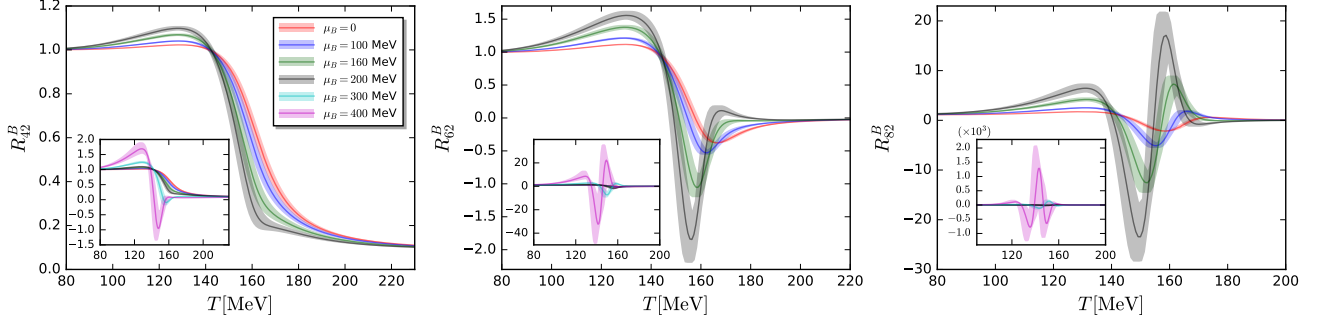


FIG. 6. R_{42}^B (left panel), R_{62}^B (middle panel), and R_{82}^B (right panel) as functions of the temperature at several values of μ_B , computed from LEFT within the fRG approach. Insets in each plot show their respective zoom-out view.

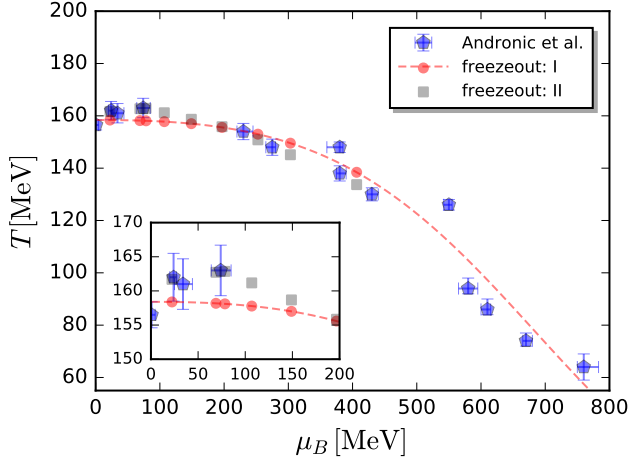


FIG. 7. Chemical freeze-out temperature and baryon chemical potential in the $T - \mu_B$ plane. The blue points show the freeze-out data from Andronic *et al.* in [50]. The red circles and dashed line represent the freeze-out temperature obtained from the parametrization of blue points through Eq. (35), which are denoted as the freeze-out: I in this work. The gray squares represent the freeze-out temperature obtained from interpolation of blue points, which are denoted as the freeze-out: II. The inlay zooms in the low- μ_B region.

theoretical results are confronted with experiments, but rather assume that the measured cumulants of the net-proton multiplicity distribution at a given collision energy, with other collision parameters e.g., the centrality and rapidity range fixed, is in one-by-one correspondence to the calculated fluctuations in Eq. (19) with one value of T or μ_B . It is reasonable to attribute the values of T and μ_B to be the ones when the chemical freeze-out occurs, viz. T_{CF} and $\mu_{B_{CF}}$. Such an approach for the comparison is usually employed in fluctuation studies of equilibrium QCD matter within functional methods or lattice simulations [45, 57, 58]. Note, however, that because of the reasons we have outlined above, results of comparison between the theory and experiment within

this simplified approach should be taken with a grain of salt. In this work we adopt the commonly used freeze-out temperature and baryon chemical potential in [50], which are obtained from the analysis of hadron yields in a hadron resonance gas model, as shown by the blue points in Fig. 7. Relevant freeze-out data have also been parameterized [50] and, e.g., the dependence of freeze-out chemical potential on the collision energy is given by

$$\mu_{B_{CF}} = \frac{a}{1 + 0.288\sqrt{s_{NN}}}, \quad (34)$$

with $a = 1307.5$ MeV, which is used in this work to determine $\mu_{B_{CF}}$ for every $\sqrt{s_{NN}}$. For the freeze-out temperature, we adopt two approaches. One is to use directly the parameterized chemical freeze-out temperature, which reads

$$T_{CF} = \frac{T_{CF}^{lim}}{1 + \exp(2.60 - \ln(\sqrt{s_{NN}}/0.45))}, \quad (35)$$

and the relevant result as a function of $\mu_{B_{CF}}$ is shown by the red dashed line in Fig. 7, and those corresponding to different collision energy are shown by red circles. The freeze-out temperature determined in Eq. (35) is denoted as the freeze-out: I in this work. Moreover, we also use another approach to determine the freeze-out temperature for different values of $\sqrt{s_{NN}}$, to wit, interpolating it among the blue points in Fig. 7, and the relevant results are shown by the gray squares, which is denoted as freeze-out: II in the following. Freeze-out temperature for freeze-out: I and freeze-out: II, as well as the freeze-out baryon chemical potential, with different center-of-mass energy per nucleon pair $\sqrt{s_{NN}}$ are presented in Tab. I. One can see that the difference of freeze-out temperature between freeze-out: I and freeze-out: II is as large as ~ 5 MeV, which is large enough to allow us to study the error of calculations stemming from the determination of T_{CF} .

In Fig. 8 we show the dependence of baryon number fluctuations R_{42}^B , R_{62}^B , and R_{82}^B on the center-of-mass collision energy, which is calculated in the LEFT within the fRG approach with the freeze-out: I and freeze-out: II as

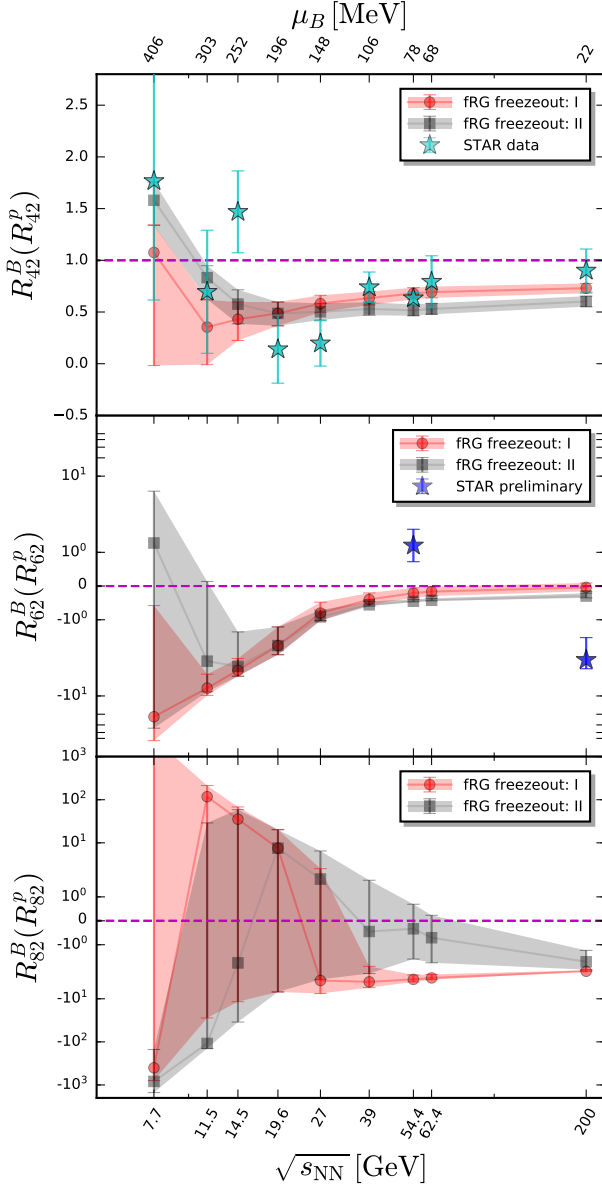


FIG. 8. Baryon number fluctuations R_{42}^B (top), R_{62}^B (middle), and R_{82}^B (bottom) as functions of the collision energy, calculated in LEFT within the fRG approach with the freeze-out: I and freeze-out: II, respectively. Experimental data from the STAR collaboration are also shown for comparison, where R_{42}^p (top) are the kurtosis of the net-proton distributions measured in Au+Au central (0-5%) collisions [7], and R_{62}^p (middle) is the preliminary result on the six-order cumulant of the net-proton distribution at $\sqrt{s_{NN}}=200$ GeV and 54.4 GeV with centrality 0-40% [13, 14]. The horizontal dashed lines indicate positions of unity for $R_{42}^B(R_{42}^p)$, zeros for $R_{62}^B(R_{62}^p)$ and R_{82}^B .

shown in Tab. I, respectively. The theoretical results are also confronted with experimental measurement of cumulants of the net-proton distributions in the beam energy scan experiments from the STAR collaboration. The kurtosis of the net-proton distributions R_{42}^p are measured in Au+Au collisions with centrality 0-5%, transverse mo-

mentum range $0.4 < p_T \text{ (GeV/c)} < 2.0$, and rapidity $|y| < 0.5$, cf. [7] for more details. Moreover, preliminary results for the six-order cumulant of the net-proton distribution R_{62}^p are also presented in the middle plot of Fig. 8, which are obtained at two values of the collision energy, i.e., $\sqrt{s_{NN}}=200$ GeV and 54.4 GeV with centrality 0-40% [13, 14].

As shown in Fig. 8, the theoretical result of the fourth-order fluctuation calculated in the fRG-LEFT approach is in qualitative agreement with the experimental measurement of the kurtosis of net-proton distributions. In particular, a nonmonotonic behavior in the low collision energy regime, say below ~ 20 GeV, is also found in the fRG calculation with both freeze-out lines, which reveals that the strength of the chiral crossover is increased rapidly in this region. Moreover, the nonmonotonic behavior is also observed in the sixth-order and eighth-order baryon number fluctuations as functions of the collision energy. However, it should be noted that the errors of both R_{42}^B and R_{62}^B within the fRG approach, as indicated by the red and gray bands in Fig. 8, increase significantly in the low energy region, and the situation becomes even worse in the case of R_{82}^B . The red or gray error bands in Fig. 8 indicate the systematic errors of theoretical calculation in the fRG-LEFT approach, which stem from errors in the scale matching as encoded in the coefficients c_T and c_μ in Eq. (27). Comparing the red bands with the gray ones, one finds that errors of the freeze-out temperature lead to significant errors of baryon number fluctuations predicted in the low collision energy regime, and hence a determination of freeze-out temperature with high precision in the region is highly required in the future. It is also of interest to compare theoretical and experimental results for the six-order baryon or proton fluctuations, which is accessible for two values of collision energy, i.e., $\sqrt{s_{NN}}=200$ GeV and 54.4 GeV. One observes that there has been yet a remarkable deviation between the theory and experiment. However, we find that, for the highest collision energy $\sqrt{s_{NN}}=200$ GeV, the value of R_{62}^B within the fRG approach is negative though very close to zero, which is qualitatively consistent with the experimental measurement.

V. SUMMARY AND OUTLOOK

ACKNOWLEDGMENTS

The work was supported by the National Natural Science Foundation of China under Contracts Nos. 11775041.

Appendix A: Glue potential

As we have discussed in Sec. II, the dynamics of the glue sector in QCD is partly imprinted in the glue potential $V_{\text{glue},k}(A_0)$, cf. Eq. (3), when the RG scale is in the

regime of LEFT. We neglect the scale dependence of the glue potential in this work, and assume

$$V_{\text{glue}}(L, \bar{L}) = V_{\text{glue}, k=0}(A_0) = T^4 \bar{V}_{\text{glue}}(L, \bar{L}), \quad (\text{A1})$$

where we have introduced a dimensionless glue potential \bar{V}_{glue} , and its dependence on the temporal background A_0 field is realized via the traced Polyakov loop L and its conjugate \bar{L} , which reads

$$L(\mathbf{x}) = \frac{1}{N_c} \langle \text{Tr } \mathcal{P}(\mathbf{x}) \rangle, \quad \bar{L}(\mathbf{x}) = \frac{1}{N_c} \langle \text{Tr } \mathcal{P}^\dagger(\mathbf{x}) \rangle, \quad (\text{A2})$$

with

$$\mathcal{P}(\mathbf{x}) = \mathcal{P} \exp \left(ig \int_0^\beta d\tau \hat{A}_0(\mathbf{x}, \tau) \right), \quad (\text{A3})$$

where \mathcal{P} on the r.h.s. is the path ordering operator. In this work we adopt the parametrization of the glue potential in [59], which reads

$$V_{\text{glue}}(L, \bar{L}) = -\frac{a(T)}{2} \bar{L}L + b(T) \ln M_H(L, \bar{L}) + \frac{c(T)}{2} (L^3 + \bar{L}^3) + d(T) (\bar{L}L)^2, \quad (\text{A4})$$

with the $\text{SU}(N_c)$ Haar measure

$$M_H(L, \bar{L}) = 1 - 6\bar{L}L + 4(L^3 + \bar{L}^3) - 3(\bar{L}L)^2. \quad (\text{A5})$$

Note that the parametrization of glue potential in Eq. (A4), as well as determination of relevant parameters in Tab. II, is done based on lattice results of $\text{SU}(3)$ Yang-Mills theory at finite temperature, where not only the expectation value of the Polyakov loop and pressure, but also quadratic fluctuations of the Polyakov loop are taken into account [59]. The coefficients in Eq. (A4) are dependent on the temperature, which reads

$$x(T) = \frac{x_1 + x_2/(t_r + 1) + x_3/(t_r + 1)^2}{1 + x_4/(t_r + 1) + x_5/(t_r + 1)^2}, \quad (\text{A6})$$

for $x \in \{a, c, d\}$, and

$$b(T) = b_1(t_r + 1)^{-b_4} \left(1 - e^{b_2/(t_r+1)^{b_3}} \right), \quad (\text{A7})$$

with the reduced temperature $t_r = (T - T_c)/T_c$, and the parameters in Eq. (A6) and Eq. (A7) have been fixed in [59] and their values are also collected in Tab. II for convenience.

Though the parametrization of the glue potential in Eq. (A4) is based on results of the Yang-Mills theory, it has found that the unquenching effect in QCD is well captured, once a linear rescaling of the reduced temperature is made from the pure gauge theory to QCD [60–62], as follows

$$(t_r)_{\text{YM}} \rightarrow \alpha (t_r)_{\text{glue}}, \quad (\text{A8})$$

with

$$(t_r)_{\text{glue}} = (T - T_c^{\text{glue}})/T_c^{\text{glue}}, \quad (\text{A9})$$

where we have used $\alpha = 0.7$ and $T_c^{\text{glue}} = 216$ MeV (in unit of physical temperature via Eq. (27)) in this work.

	1	2	3	4	5
a_i	-44.14	151.4	-90.0677	2.77173	3.56403
b_i	-0.32665	-82.9823	3.0	5.85559	
c_i	-50.7961	114.038	-89.4596	3.08718	6.72812
d_i	27.0885	-56.0859	71.2225	2.9715	6.61433

TABLE II. Values of the parameters in (A6) and (A7) for the glue potential.

Appendix B: Flow equations

The flow equation for the effective potential of the matter sector is given in Eq. (10). In this work we use the Taylor expansion approach to solve this equation numerically. Expanding the potential around a k -dependent value κ_k , one arrives at

$$V_{\text{mat},k}(\rho) = \sum_{n=0}^{N_v} \frac{\lambda_{n,k}}{n!} (\rho - \kappa_k)^n, \quad (\text{B1})$$

with the expansion coefficients $\lambda_{n,k}$'s, where N_v is the maximal order of Taylor expansion included in the numerical calculation. It is more convenient to rewrite Eq. (B1) by means of the renormalized variables, i.e.,

$$\bar{V}_{\text{mat},k}(\bar{\rho}) = \sum_{n=0}^{N_v} \frac{\bar{\lambda}_{n,k}}{n!} (\bar{\rho} - \bar{\kappa}_k)^n, \quad (\text{B2})$$

with $\bar{V}_{\text{mat},k}(\bar{\rho}) = V_{\text{mat},k}(\rho)$, $\bar{\rho} = Z_{\phi,k}\rho$, $\bar{\kappa}_k = Z_{\phi,k}\kappa_k$, and $\bar{\lambda}_{n,k} = \lambda_{n,k}/(Z_{\phi,k})^n$. Inserting Eq. (B2) into the l.h.s. of Eq. (10) leads us to

$$\begin{aligned} & \left. \partial_{\bar{\rho}}^n \left(\partial_t \bar{V}_{\text{mat},k}(\bar{\rho}) \right) \right|_{\bar{\rho}=\bar{\kappa}_k} \\ &= (\partial_t - n\eta_{\phi,k}) \bar{\lambda}_{n,k} - (\partial_t \bar{\kappa}_k + \eta_{\phi,k} \bar{\kappa}_k) \bar{\lambda}_{n+1,k}. \end{aligned} \quad (\text{B3})$$

In our calculation, the expansion point κ_k in Eq. (B1) or $\bar{\kappa}_k$ in Eq. (B2) is chosen such that it is the minimum of the effective action in Eq. (2), which yields the equation of motion as follows

$$\left. \frac{\partial}{\partial \bar{\rho}} \left(\bar{V}_{\text{mat},k}(\bar{\rho}) - \bar{c}_k \bar{\sigma} \right) \right|_{\bar{\rho}=\bar{\kappa}_k} = 0, \quad (\text{B4})$$

with $\bar{\sigma} = Z_{\phi,k}^{1/2} \sigma$ and $\bar{c}_k = Z_{\phi,k}^{-1/2} c$, where c is independent of the IR cutoff k . This expansion is usually called the physical running expansion, since the bare expansion point κ_k is k -dependent as mentioned above. In contrast, another commonly used expansion approach is the fixed-point expansion, and as its name suggests, in this approach the bare expansion point is k -independent. For more discussions about these two different expansion approaches, and their advantages and disadvantages in the application of fRG calculations, see e.g., [19, 41, 63–65].

Combination of Eq. (B3) and Eq. (B4) leaves us with the flow equation for the expansion point, which reads

$$\partial_t \bar{\kappa}_k = -\frac{\bar{c}_k^2}{\bar{\lambda}_{1,k}^3 + \bar{c}_k^2 \bar{\lambda}_{2,k}^2} \left[\partial_{\bar{\rho}} \left(\partial_t \big|_{\rho} \bar{V}_{\text{mat},k}(\bar{\rho}) \right) \bigg|_{\bar{\rho}=\bar{\kappa}_k} + \eta_{\phi,k} \left(\frac{\bar{\lambda}_{1,k}}{2} + \bar{\kappa}_k \bar{\lambda}_{2,k} \right) \right]. \quad (\text{B5})$$

The meson anomalous dimension in Eq. (14) reads

$$\eta_{\phi,k} = \frac{1}{6\pi^2} \left\{ \frac{4}{k^2} \bar{\kappa}_k (\bar{V}_k''(\bar{\kappa}_k))^2 \mathcal{B}\mathcal{B}_{(2,2)}(\tilde{m}_{\pi,k}^2, \tilde{m}_{\sigma,k}^2; T) + N_c \bar{h}_k^2 \left[\mathcal{F}_{(2)}(\tilde{m}_{q,k}^2; T, \mu)(2\eta_{q,k} - 3) - 4(\eta_{q,k} - 2) \mathcal{F}_{(3)}(\tilde{m}_{q,k}^2; T, \mu) \right] \right\}, \quad (\text{B6})$$

The quark anomalous dimension in Eq. (15) reads

$$\eta_{q,k} = \frac{1}{24\pi^2 N_f} (4 - \eta_{\phi,k}) \bar{h}_k^2 \times \left\{ (N_f^2 - 1) \mathcal{F}\mathcal{B}_{(1,2)}(\tilde{m}_{q,k}^2, \tilde{m}_{\pi,k}^2; T, \mu, p_{0,ex}) + \mathcal{F}\mathcal{B}_{(1,2)}(\tilde{m}_{q,k}^2, \tilde{m}_{\sigma,k}^2; T, \mu, p_{0,ex}) \right\}, \quad (\text{B7})$$

where in the threshold function $\mathcal{F}\mathcal{B}$'s we have employed $p_{0,ex} = \pi T$ for the finite temperature sector and $p_{0,ex} = \pi T \exp\{-k/(\pi T)\}$ for the vacuum sector. The modification for the vacuum sector is necessitated in order to suppress the artefact of temperature dependence of thermodynamics in the low temperature region [64], which

can be resolved by means of frequency summation of the quark external leg [42]. The flow of the Yukawa coupling in Eq. (16) is given by

$$\partial_t \bar{h}_k = \left(\frac{1}{2} \eta_{\phi,k} + \eta_{q,k} \right) \bar{h}_k(\bar{\rho}) + \frac{\bar{h}_k^3}{4\pi^2 N_f} \left[L_{(1,1)}^{(4)}(\tilde{m}_{q,k}^2, \tilde{m}_{\sigma,k}^2, \eta_{q,k}, \eta_{\phi,k}; T, \mu, p_{0,ex}) - (N_f^2 - 1) L_{(1,1)}^{(4)}(\tilde{m}_{q,k}^2, \tilde{m}_{\pi,k}^2, \eta_{q,k}, \eta_{\phi,k}; T, \mu, p_{0,ex}) \right]. \quad (\text{B8})$$

Note that explicit expressions of all the threshold functions mentioned above, such as $\mathcal{B}\mathcal{B}$, \mathcal{F} 's, $\mathcal{F}\mathcal{B}$'s, and L can be found in e.g., [4, 41].

To summarize, flow equations (10), (B3), (B5), (B8) supplemented with Eq. (B6) and Eq. (B7) constitute a closed set of ordinary differential equations, which is evolved from the UV cutoff $k = \Lambda$ to the IR limit $k = 0$. The parameters of LEFT are given by initial values of the flow equations. To be specific, the effective potential of the matter sector at the UV cutoff reads

$$V_{\text{mat},k=\Lambda}(\rho) = \frac{\lambda_{k=\Lambda}}{2} \rho^2 + \nu_{k=\Lambda} \rho, \quad (\text{B9})$$

with $\lambda_{k=\Lambda} = 11$ and $\nu_{k=\Lambda} = (0.830 \text{ GeV})^2$. In addition, the initial value of the Yukawa coupling is $h_{k=\Lambda} = 10.18$, and the explicit chiral symmetry breaking parameter is $c = 2.82 \times 10^{-3} \text{ GeV}^3$. These parameters are fixed by fitting the hadronic observables in vacuum, i.e., $f_\pi = 92 \text{ MeV}$, $m_q = 306 \text{ MeV}$, $m_\pi = 136 \text{ MeV}$, and $m_\sigma = 483 \text{ MeV}$.

-
- [1] X. Luo and N. Xu, Nucl. Sci. Tech. **28**, 112 (2017), arXiv:1701.02105 [nucl-ex].
 - [2] A. Bzdak, S. Esumi, V. Koch, J. Liao, M. Stephanov, and N. Xu, Phys. Rept. **853**, 1 (2020), arXiv:1906.00936 [nucl-th].
 - [3] C. S. Fischer, Prog. Part. Nucl. Phys. **105**, 1 (2019), arXiv:1810.12938 [hep-ph].
 - [4] W.-j. Fu, J. M. Pawłowski, and F. Rennecke, Phys. Rev. D **101**, 054032 (2020), arXiv:1909.02991 [hep-ph].
 - [5] M. A. Stephanov, *Proceedings, 24th International Symposium on Lattice Field Theory (Lattice 2006): Tucson, USA, July 23-28, 2006*, PoS **LAT2006**, 024 (2006), arXiv:hep-lat/0701002 [hep-lat].
 - [6] M. Stephanov, Phys. Rev. Lett. **102**, 032301 (2009), arXiv:0809.3450 [hep-ph].
 - [7] J. Adam *et al.* (STAR), (2020), arXiv:2001.02852 [nucl-ex].
 - [8] L. Adamczyk *et al.* (STAR), Phys. Rev. Lett. **112**, 032302 (2014), arXiv:1309.5681 [nucl-ex].
 - [9] L. Adamczyk *et al.* (STAR), Phys. Rev. Lett. **113**, 092301 (2014), arXiv:1402.1558 [nucl-ex].
 - [10] X. Luo (STAR), *Proceedings, 9th International Workshop on Critical Point and Onset of Deconfinement (CPOD 2014): Bielefeld, Germany, November 17-21, 2014*, PoS **CPOD2014**, 019 (2015), arXiv:1503.02558 [nucl-ex].
 - [11] L. Adamczyk *et al.* (STAR), Phys. Lett. **B785**, 551 (2018), arXiv:1709.00773 [nucl-ex].
 - [12] J. Adam *et al.* (STAR), Phys. Rev. C **100**, 014902 (2019), arXiv:1903.05370 [nucl-ex].
 - [13] T. Nonaka (STAR), in *28th International Conference on Ultrarelativistic Nucleus-Nucleus Collisions* (2020) arXiv:2002.12505 [nucl-ex].
 - [14] A. Pandav (STAR), (2020), arXiv:2003.12503 [nucl-ex].
 - [15] C. Wetterich, Phys. Lett. **B301**, 90 (1993).

- [16] U. Ellwanger, *Proceedings, Workshop on Quantum field theoretical aspects of high energy physics: Bad Frankenhausen, Germany, September 20-24, 1993*, Z. Phys. **C62**, 503 (1994), [,206(1993)], arXiv:hep-ph/9308260 [hep-ph].
- [17] T. R. Morris, Int. J. Mod. Phys. **A9**, 2411 (1994), arXiv:hep-ph/9308265 [hep-ph].
- [18] M. Mitter, J. M. Pawłowski, and N. Strodthoff, Phys. Rev. **D91**, 054035 (2015), arXiv:1411.7978 [hep-ph].
- [19] J. Braun, L. Fister, J. M. Pawłowski, and F. Rennecke, Phys. Rev. **D94**, 034016 (2016), arXiv:1412.1045 [hep-ph].
- [20] A. K. Cyrol, M. Mitter, J. M. Pawłowski, and N. Strodthoff, Phys. Rev. **D97**, 054006 (2018), arXiv:1706.06326 [hep-ph].
- [21] J. Braun, H. Gies, and J. M. Pawłowski, Phys. Lett. **B684**, 262 (2010), arXiv:0708.2413 [hep-th].
- [22] J. Braun, Eur. Phys. J. **C64**, 459 (2009), arXiv:0810.1727 [hep-ph].
- [23] J. Braun, L. M. Haas, F. Marhauser, and J. M. Pawłowski, Phys. Rev. Lett. **106**, 022002 (2011), arXiv:0908.0008 [hep-ph].
- [24] A. K. Cyrol, L. Fister, M. Mitter, J. M. Pawłowski, and N. Strodthoff, Phys. Rev. **D94**, 054005 (2016), arXiv:1605.01856 [hep-ph].
- [25] A. K. Cyrol, M. Mitter, J. M. Pawłowski, and N. Strodthoff, Phys. Rev. **D97**, 054015 (2018), arXiv:1708.03482 [hep-ph].
- [26] J. Braun, W.-j. Fu, J. M. Pawłowski, F. Rennecke, D. Rosenblüh, and S. Yin, (2020), arXiv:2003.13112 [hep-ph].
- [27] J. Berges, N. Tetradis, and C. Wetterich, Phys. Rept. **363**, 223 (2002), arXiv:hep-ph/0005122 [hep-ph].
- [28] J. M. Pawłowski, Annals Phys. **322**, 2831 (2007), arXiv:hep-th/0512261 [hep-th].
- [29] B.-J. Schaefer and J. Wambach, *Helmholtz International Summer School on Dense Matter in Heavy Ion Collisions and Astrophysics Dubna, Russia, August 21-September 1, 2006*, Phys. Part. Nucl. **39**, 1025 (2008), arXiv:hep-ph/0611191 [hep-ph].
- [30] H. Gies, *Renormalization group and effective field theory approaches to many-body systems*, Lect. Notes Phys. **852**, 287 (2012), arXiv:hep-ph/0611146 [hep-ph].
- [31] O. J. Rosten, Phys. Rept. **511**, 177 (2012), arXiv:1003.1366 [hep-th].
- [32] J. Braun, J. Phys. **G39**, 033001 (2012), arXiv:1108.4449 [hep-ph].
- [33] J. M. Pawłowski, *Proceedings, 24th International Conference on Ultra-Relativistic Nucleus-Nucleus Collisions (Quark Matter 2014): Darmstadt, Germany, May 19-24, 2014*, Nucl. Phys. **A931**, 113 (2014).
- [34] H. Gies and C. Wetterich, Phys. Rev. **D65**, 065001 (2002), arXiv:hep-th/0107221 [hep-th].
- [35] H. Gies and C. Wetterich, Phys. Rev. **D69**, 025001 (2004), arXiv:hep-th/0209183 [hep-th].
- [36] S. Floerchinger and C. Wetterich, Phys. Lett. **B680**, 371 (2009), arXiv:0905.0915 [hep-th].
- [37] K. Fukushima, Phys. Lett. **B591**, 277 (2004), arXiv:hep-ph/0310121 [hep-ph].
- [38] C. Ratti, M. A. Thaler, and W. Weise, Phys. Rev. **D73**, 014019 (2006), arXiv:hep-ph/0506234 [hep-ph].
- [39] B.-J. Schaefer, J. M. Pawłowski, and J. Wambach, Phys. Rev. **D76**, 074023 (2007), arXiv:0704.3234 [hep-ph].
- [40] W.-j. Fu, Z. Zhang, and Y.-x. Liu, Phys. Rev. **D77**, 014006 (2008), arXiv:0711.0154 [hep-ph].
- [41] S. Yin, R. Wen, and W.-j. Fu, Phys. Rev. D **100**, 094029 (2019), arXiv:1907.10262 [hep-ph].
- [42] W.-j. Fu, J. M. Pawłowski, F. Rennecke, and B.-J. Schaefer, Phys. Rev. D **94**, 116020 (2016), arXiv:1608.04302 [hep-ph].
- [43] A. Bazavov *et al.*, Phys. Rev. **D95**, 054504 (2017), arXiv:1701.04325 [hep-lat].
- [44] A. Bazavov *et al.* (HotQCD), Phys. Rev. **D96**, 074510 (2017), arXiv:1708.04897 [hep-lat].
- [45] A. Bazavov *et al.*, Phys. Rev. D **101**, 074502 (2020), arXiv:2001.08530 [hep-lat].
- [46] S. Borsanyi, Z. Fodor, J. N. Guenther, S. K. Katz, K. K. Szabo, A. Pasztor, I. Portillo, and C. Ratti, JHEP **10**, 205 (2018), arXiv:1805.04445 [hep-lat].
- [47] A. Bazavov *et al.* (HotQCD), Phys. Lett. **B795**, 15 (2017), arXiv:1812.08235 [hep-lat].
- [48] R. Bellwied, S. Borsanyi, Z. Fodor, J. Guenther, S. D. Katz, C. Ratti, and K. K. Szabo, Phys. Lett. **B751**, 559 (2015), arXiv:1507.07510 [hep-lat].
- [49] S. Borsanyi, Z. Fodor, J. N. Guenther, R. Kara, S. D. Katz, P. Parotto, A. Pasztor, C. Ratti, and K. K. Szabo, (2020), arXiv:2002.02821 [hep-lat].
- [50] A. Andronic, P. Braun-Munzinger, K. Redlich, and J. Stachel, Nature **561**, 321 (2018), arXiv:1710.09425 [nucl-th].
- [51] L. Adamczyk *et al.* (STAR), Phys. Rev. **C96**, 044904 (2017), arXiv:1701.07065 [nucl-ex].
- [52] X. Luo, J. Xu, B. Mohanty, and N. Xu, J. Phys. G **40**, 105104 (2013), arXiv:1302.2332 [nucl-ex].
- [53] P. Braun-Munzinger, A. Rustamov, and J. Stachel, Nucl. Phys. A **960**, 114 (2017), arXiv:1612.00702 [nucl-th].
- [54] V. Vovchenko, O. Savchuk, R. V. Poberezhnyuk, M. I. Gorenstein, and V. Koch, (2020), arXiv:2003.13905 [hep-ph].
- [55] M. Nahrgang, M. Bluhm, P. Alba, R. Bellwied, and C. Ratti, Eur. Phys. J. C **75**, 573 (2015), arXiv:1402.1238 [hep-ph].
- [56] M. Bluhm *et al.*, (2020), arXiv:2001.08831 [nucl-th].
- [57] W.-j. Fu and J. M. Pawłowski, Phys. Rev. **D93**, 091501 (2016), arXiv:1512.08461 [hep-ph].
- [58] P. Isserstedt, M. Buballa, C. S. Fischer, and P. J. Gunkel, (2019), arXiv:1906.11644 [hep-ph].
- [59] P. M. Lo, B. Friman, O. Kaczmarek, K. Redlich, and C. Sasaki, Phys. Rev. **D88**, 074502 (2013), arXiv:1307.5958 [hep-lat].
- [60] J. M. Pawłowski, *Proceedings, 9th Conference on Quark Confinement and the Hadron Spectrum: Madrid, Spain, 30 Aug-3 Sep 2010*, AIP Conf. Proc. **1343**, 75 (2011), arXiv:1012.5075 [hep-ph].
- [61] L. M. Haas, R. Stiele, J. Braun, J. M. Pawłowski, and J. Schaffner-Bielich, Phys. Rev. **D87**, 076004 (2013), arXiv:1302.1993 [hep-ph].
- [62] T. K. Herbst, M. Mitter, J. M. Pawłowski, B.-J. Schaefer, and R. Stiele, Phys. Lett. **B731**, 248 (2014), arXiv:1308.3621 [hep-ph].
- [63] J. M. Pawłowski and F. Rennecke, Phys. Rev. **D90**, 076002 (2014), arXiv:1403.1179 [hep-ph].
- [64] W.-j. Fu and J. M. Pawłowski, Phys. Rev. **D92**, 116006 (2015), arXiv:1508.06504 [hep-ph].
- [65] F. Rennecke and B.-J. Schaefer, Phys. Rev. **D96**, 016009 (2017), arXiv:1610.08748 [hep-ph].